

# Atomic-Scale Simulations of Meteor Ablation

Gabrielle Guttormsen<sup>1</sup>, Alex C. Fletcher<sup>2</sup>, and Meers M. Oppenheim<sup>1</sup>

<sup>1</sup>Center for Space Physics, Boston University, Boston, MA, USA

<sup>2</sup>Naval Research Laboratory, Washington D.C., USA

## Key Points:

- Single particle impacts on meteoroid surfaces were simulated in 3D using molecular dynamics
- Sputtering yields for different meteoroid materials are compared to theory
- Atmospheric particles energy transfer is less than previously assumed affecting ablation models

---

Corresponding author: Gabrielle Guttormsen, [gabigutt@bu.edu](mailto:gabigutt@bu.edu)

11 **Abstract**

12 Meteoroids smaller than a microgram constantly bombard the Earth, depositing  
 13 material in the mesosphere and lower thermosphere. Meteoroid ablation, the explosive  
 14 evaporation of meteoroids due to erosive impacts of atmospheric particles, consists of sput-  
 15 tering and sublimation. This paper presents the first atomic scale modeling of sputter-  
 16 ing, the initial stage of ablation where hypersonic collisions between the meteoroid and  
 17 atmospheric particles cause the direct ejection of atoms from the meteoroid surface. Be-  
 18 cause meteoroids gain thermal energy from these particle impacts, these interactions are  
 19 important for sublimation as well. In this study, a molecular dynamics simulator calcu-  
 20 lates the energy distribution of the sputtered particles as a function of the species, ve-  
 21 locity, and angle of the incoming atmospheric particles. The sputtering yield generally  
 22 agrees with semi-empirical equations at normal incidence but disagrees with the gener-  
 23 ally accepted angular dependence.  $\Lambda$ , the fraction of energy from a single atmospheric  
 24 particle impact incorporated into the meteoroid, was found to be less than 1 and depen-  
 25 dent on the velocity, angle, atmospheric species, and meteoroid material. Applying this  
 26 new  $\Lambda$  to an ablation model results in a slower meteoroid temperature increase and mass  
 27 loss rate as a function of altitude. This alteration results in changes in the expected elec-  
 28 tron line densities and visual magnitudes of meteoroids. Notably, this analysis leads to  
 29 the prediction that meteoroids will generally ablate 1 - 4 km lower than previously pre-  
 30 dicted. This affects analysis of radar and visual measurements, as well as determination  
 31 of meteoroid mass.

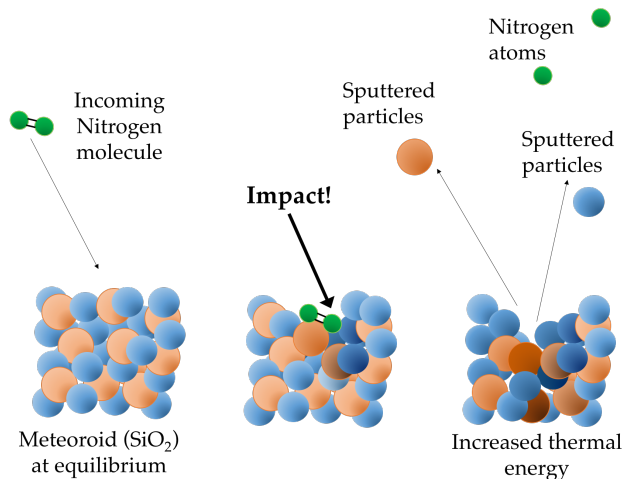
32 **1 Introduction**

33 Billions of small meteoroids vaporize in Earth's atmosphere each day. The major-  
 34 ity of these meteoroids weigh less than a milligram and have velocities ranging from 11  
 35 km/s to 72 km/s (Love & Brownlee, 1991). Meteoroids begin to lose mass (ablate) once  
 36 they collide with atmospheric particles. The neutral atmosphere becomes exponentially  
 37 denser with decreasing altitude, which exponentially increases the collision rate. The lib-  
 38 erated meteoroid atoms collide with atmospheric particles, forming plasma via collisional  
 39 ionization. Radars often observe the liberated electron.

40 There are two mechanisms for meteoroid ablation in the atmosphere: sputtering  
 41 and sublimation. Sputtering is the direct ejection of a small number of atoms from the  
 42 meteoroid due to impacts by atmospheric particles. It is the dominant ablation process  
 43 for very small and very fast meteoroids (Rogers et al., 2005). Sublimation occurs when  
 44 the meteoroid reaches a sufficiently high temperature ( $\gtrsim 2200$  K) and dominates the mass  
 45 loss (Ceplecha et al., 1998). However, the single particle impacts influence the heating  
 46 rate of the meteoroid, which determines when the sublimation rate as well. Fig. 1 de-  
 47 picts an example of this process.

51 Each impact by an atmospheric particle on the meteoroid surface has a chance to  
 52 dislodge (sputter) a small number of meteoroid atoms (on average 0, 1, or 2 atoms per  
 53 impact, depending on meteoroid velocity). These sputtered particles carry away energy  
 54 from the meteoroid. The incident atmospheric particle therefore transfers some, but gen-  
 55 erally not all, of its kinetic energy to the meteoroid in the form of increased thermal en-  
 56 ergy. The fraction of kinetic energy that is converted to thermal energy, averaged over  
 57 many impacts, is the energy transfer coefficient,  $\Lambda$ . This coefficient is a function of me-  
 58 teoroid velocity, shape, and the material makeup of the meteoroid and atmosphere (which  
 59 changes with altitude). Most ablation models assume  $\Lambda = 1$  (e.g. Rogers et al., 2005;  
 60 Vondrak et al., 2008; Briani et al., 2013), and this assumption will overestimate the heat-  
 61 ing rate and therefore the mass loss rate from sublimation.

62 In this paper, we use atomic scale molecular dynamics (MD) simulations to model  
 63 impacts of atmospheric particles on meteoroid surfaces. We consider a range of mete-



48 **Figure 1.** This image shows a nitrogen molecule from the atmosphere striking a stony meteoroid. Two atoms from the meteoroid are sputtered and the thermal energy of the meteoroid  
 49  
 50 body increases.

64 oroid velocities, impact angles, meteoroid materials, and incident atmospheric particles.  
 65 We simulate each type of impact hundreds of times in order to determine average sput-  
 66 tering yields (which is the number of atoms leaving the surface meteoroid due to a sin-  
 67 gle impact), the energy distribution of sputtered particles, and the energy transfer co-  
 68 efficient ( $\Lambda$ ). The microscopic simulation data provides macroscopic coefficients neces-  
 69 sary for meteoroid ablation models. We then show how a reduced energy transfer coef-  
 70 ficient ( $\Lambda < 1$ ) affects the mass loss rate, as well as derived radar/optical observables  
 71 (Campbell-Brown & Koschny, 2004; Szasz et al., 2008; Vida et al., 2018; Dimant & Op-  
 72 penheim, 2017a, 2017b).

73 Models assume  $\Lambda = 1.0$ , so energy from atmospheric impacting atmospheric particles  
 74 is completely incorporated into the meteoroid (Lebedinets & Shushkova, 1970; Ce-  
 75 plecha et al., 1998; Rogers et al., 2005; Hill et al., 2005). Others assume that half the  
 76 initial energy is transferred to the meteoroid (Campbell-Brown & Koschny, 2004; Vida et  
 77 al., 2018). Models that fit to data use a range of values from 0.2-1.0 (Szasz et al., 2008;  
 78 Thomas, 2017). Briani et al. (2013) calculate the  $\Lambda$  as an output of their numerical model  
 79 (0.9 for low velocities) and Popova, Strelkov, and Sidneva (2007) calculates  $\Lambda$  with en-  
 80 ergy ratios from Monte-Carlo simulations, finding  $\Lambda$  between 0.75 and 1.0. Experimen-  
 81 tally, DeLuca and Sternovsky (2019) used a measured drag coefficient to constrain the  
 82 energy transfer coefficient to  $\Lambda = 0.58 \pm 0.37$  for a low velocity aluminum target in air.  
 83 MD simulations with physical interatomic potentials can provide an estimate for the en-  
 84 ergy transfer coefficient as well, and this is the subject of the paper.

85 Researchers have used analytic theory, experiments, and simulations to study sput-  
 86 tering. A combination of analytic theory with some experimentally-determined coeffi-  
 87 cients yields a semi-analytic model for sputtering yield (e.g. Tielens et al., 1994). Ex-  
 88 perimentalists determine sputtering yield by measuring crater depth (Laegreid & Wehner,  
 89 1961; Cheney et al., 1963; Krebs, 1977; Tsunoyama et al., 1976) or by using quartz crys-  
 90 tal microbalance to detect changes in resonant frequencies that relate to the mass loss  
 91 (Varga et al., 1997; Bouneau et al., 2002; Zoerb et al., 2005). Urbassek (1997) and Behrisch  
 92 and Eckstein (2007) review the use of MD simulations to study sputtering. Most prior  
 93 sputtering simulation work focuses on the detailed dynamics of the atoms in the target

94 material. The novel aspects of this paper are the use of MD simulations to 1) determine  
95 the energy transfer coefficient, and 2) to apply the results to meteoroid ablation.

96 This paper is split into two parts. The first delves into microscopic simulations and  
97 the second applies the results from atomic-scale simulations to macroscopic meteor  
98 ablation models. The microscopic simulations use molecular dynamics (MD) simulations  
99 to model atmospheric impacts on the surface of meteoroids and extract the sputtering  
100 yield, energies of sputtered atoms, and energy transfer efficiency. The macroscopic me-  
101 teor ablation modeling uses parameters determined from the microscopic simulations to  
102 quantify changes in meteoroid temperature, mass loss, and derived parameters relevant  
103 for radar and optical observations.

## 104 2 Simulations of Meteoroid-Atmosphere Interactions

105 Molecular dynamics (MD) is a useful tool for simulating the interaction of incident  
106 atmospheric particles with a meteoroid surface. MD is extremely small scale since ev-  
107 ery atom is simulated directly. Interatomic potentials provide forces for moving the atoms  
108 at each time step. We use the Large-scale Atomic/Molecular Massively Parallel Simu-  
109 lator (LAMMPS) (Sandia National Labs & Temple University, 2013; S. Plimpton, 1995;  
110 S. J. Plimpton & Thompson, 2012).

111 From the simulations, we can determine the sputtering yield (which is how many  
112 meteoroid particles are ejected per impacting particle), the energy distribution of sput-  
113 tered particles, and the energy transfer coefficient ( $\Lambda$ , which is the fraction of kinetic en-  
114 ergy that impacting particles deposit into the meteoroid as thermal energy). The energy  
115 transfer coefficient affects the heating rate of the meteoroid, and thus the temperature,  
116 mass loss (during both sputtering and sublimation), and ultimately the radar and op-  
117 tical observables of meteors.

### 118 2.1 Simulation Setup

119 Simulation of a the single impact of an atmospheric molecule requires two steps:  
120 1) creating a meteoroid target in equilibrium, and 2) bombarding that target with at-  
121 mospheric particles. To create a meteoroid target in equilibrium, a 3D periodic box is  
122 constructed with atoms in an appropriate crystal structure at zero Kelvin. The simu-  
123 lation is run with an isenthalpic integrator ("NPH" in LAMMPS) with a Langevin ther-  
124 mostat to gradually heat the target to 250 K. The boundaries are allowed to expand and  
125 contract as necessary. After the simulation reaches thermal equilibrium at 250 K for the  
126 periodic system, one boundary is changed to vacuum and the integration is changed to  
127 be energy conserving ("NVE" in LAMMPS) in order to form the surface that the atmo-  
128 spheric particle will hit, and run until the simulation reaches equilibrium again.

129 The equilibrium meteoroid target is used in a variety of impact simulations with  
130 different atmospheric particles hitting different locations at different angles. Because sput-  
131 tering is a stochastic process, a large number of impact simulations provides statistics  
132 and allows us to determine the sputtering yield and energy transfer coefficient on aver-  
133 age.

134 These simulations used two interatomic potentials to model the atomic forces. The  
135 target lattice atoms/molecules (Fe, SiO<sub>2</sub>) respond to the Tersoff potential (Tersoff, 1988),  
136 a many-body potential suited to empirical simulations of solid, bonded materials (Müller  
137 et al., 2007; Munetoh et al., 2007). The Embedded Atom Method (EAM) potential is  
138 often used for metallic alloys like meteoroid iron. However, EAM has problems properly  
139 describing surfaces (Zhou & Huang, 2013), and microscopic surface effects dominate the  
140 sputtering process. The Tersoff potential is mainly used for covalent bonds and is an ap-  
141 propriate potential for the quartz lattice. The impacting particles (N<sub>2</sub>, O<sub>2</sub>, Ar) and the

142 target lattice interact via the Lennard-Jones potential, due to its simplicity (Behrisch  
 143 & Eckstein, 2007; Elliott, 2018). Lorentz-Berthelot combining rules determine the mixed  
 144 parameters for unlike atoms (Lorentz, 1881; Berthelot, 1898).

## 145 2.2 Sputtering Yield at Normal Incidence

146 We first examine the sputtering yield, which is the number of sputtered particles  
 147 per impacting particle, for impacts at normal incidence. Impact simulations consisted  
 148 of 256 runs for each velocity and combination of incident atmospheric particle and me-  
 149 teoroid material. The impacting particles are nitrogen (N<sub>2</sub>), oxygen (O<sub>2</sub>), and Argon (Ar).  
 150 N<sub>2</sub> and O<sub>2</sub> are the most common molecules in the region where meteoroids ablate. Ar-  
 151 gon is a trace particle in the atmosphere, but it has a large sputtering yield, is easier to  
 152 model than molecules, and has been used for some ground-based experiments. There-  
 153 fore, it is useful for examining the validity of the simulation results, and is also included.  
 154 Each impact simulation begins with the identical iron or quartz equilibrium target.

155 A single particle is deposited above the target at a random location at one of five  
 156 velocities: 23.2, 35.4, 47.6, 59.8, or 72.0 km/s. Velocities less than 22 km/s are not use-  
 157 ful to simulate for their sputtering yield, as it is close to null. For the thermal energy  
 158 transfer discussed in Section 2.5, 11 km/s impacts help determine the energy transfer  
 159 coefficient, but those simulations are not included in this section.

160 The simulations run for 0.25 to 4 ps with a variable time-step. This duration is long  
 161 enough to ensure that atoms ejected from the meteoroid surface are recorded (Behrisch  
 162 & Eckstein, 2007). Fig. 2 shows one instance of an impact simulation, and animated in  
 163 supporting information. The kinetic energy of the atoms near the impact site have in-  
 164 creased - i.e. the thermal energy of the meteoroid has increased. While the increased en-  
 165 ergy in the meteoroid is localized on these extremely short time scales, Vondrak et al.  
 166 (2008) argued that over the ablation time scale, meteoroids may be considered isother-  
 167 mal. There are a handful of atoms that have escaped the surface and will leave the do-  
 168 main at the top of the z-axis.

A widely used semi-analytic equation for sputtering yield at normal incidence is  
 (Tielens et al., 1994)

$$Y(E_0, \theta = 0) = \frac{3.56}{U_0(\text{eV})} \frac{M_1}{M_1 + M_2} \frac{Z_1 Z_2}{\sqrt{Z_1^{\frac{2}{3}} + Z_2^{\frac{2}{3}}}} s_n(\gamma) \alpha \frac{R_p}{R} \left[ 1 - \left( \frac{E_{th}}{E_0} \right)^{2/3} \right] \left( 1 - \frac{E_{th}}{E_0} \right)^2, \quad (1)$$

where  $Y$  is the yield,  $U_0$  is the sublimation energy in eV, and  $Z_1$ ,  $Z_2$ ,  $M_1$  and  $M_2$  are  
 the atomic numbers and atomic masses of the atmospheric (1) and meteoroid (2) par-  
 ticles, respectively.  $E_0$  is the kinetic energy of the impacting particle and  $E_{th}$  is the thresh-  
 old energy for sputtering related to mass ratios of  $M_1$  and  $M_2$  (Bohdansky, 1984).  $E_{th}$   
 must be greater than  $E_0$  for sputtering to occur (Bohdansky, 1984; Behrisch & Eckstein,  
 2007). The function  $s_n(\gamma)$  describes the screened Coulomb interactions (Matsunami et  
 al., 1981),

$$s_n(\gamma) = \frac{3.411\sqrt{\gamma}\ln(\gamma + 2.718)}{1 + 6.35\sqrt{\gamma} + \gamma(-1.708 + 6.882)\sqrt{\gamma}}, \quad (2)$$

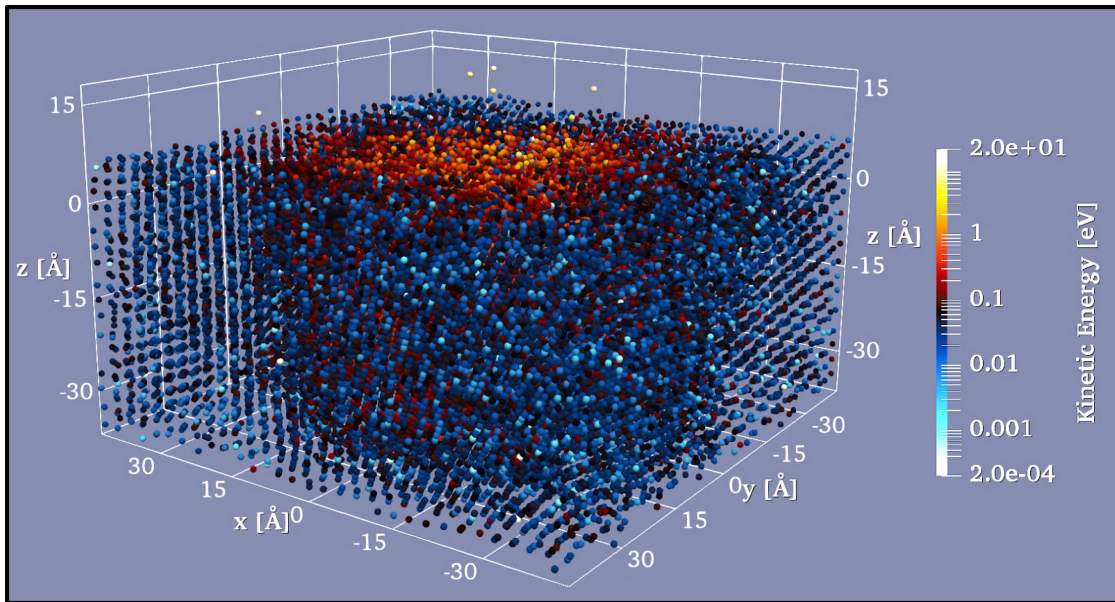
where  $\gamma$  is defined as,

$$\gamma = \frac{M_2}{M_1 + M_2} \frac{a}{Z_1 Z_2 e^2} E_0. \quad (3)$$

The functional form for  $\alpha$  is

$$\alpha = \begin{cases} 0.2 & M_2/M_1 \leq 0.5 \\ 0.3(M_2/M_1)^{2/3} & 0.5 < M_2/M_1 < 10 \end{cases} \quad (4)$$

175 Finally,  $R_p/R$  is a correction factor that mitigates the overestimation of deposited en-  
 176 ergy on the surface layer induced by  $\alpha$  for light atmospheric particles, and is the ratio  
 177 of the mean projected range to the mean penetrated path length (Bohdansky, 1984).



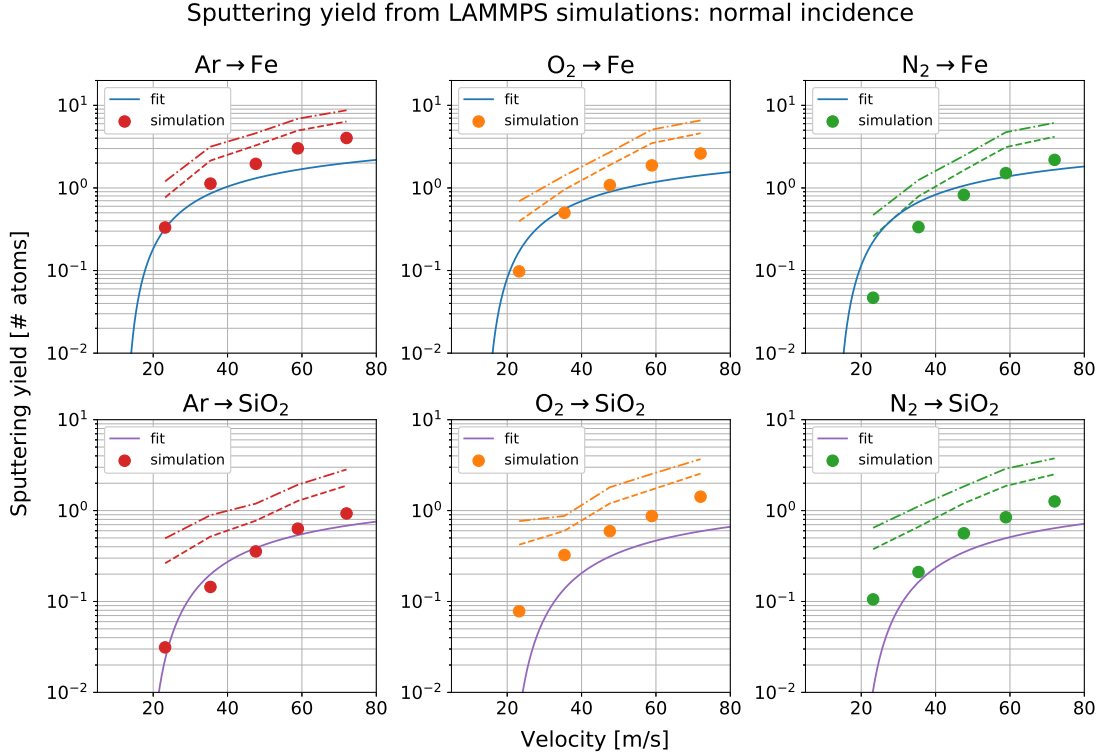
169 **Figure 2.** Snapshot of a simulation shortly after impact of a argon atom striking an iron  
 170 meteoroid surface at 72 km/s. The impact site in this case is at  $(x, y) = (0, 0)$  and the incident  
 171 molecule is normal to the surface. Only a small part of the domain is shown; the boundaries are  
 172 farther away than shown in this snapshot. The impacting molecule sputtered a handful of atoms  
 173 from the meteoroid and increased the kinetic energy of the meteoroid atoms in the vicinity of the  
 174 impact site.

178 Fig. 3 shows the sputtering yields for the atmospheric particles impacting iron in  
 179 the first row and quartz in the second, calculated over 256 simulations. The red lines in  
 180 the figure denote one and two standard deviations above the mean, representing the nat-  
 181 ural spread in the number of sputtered atoms over different simulation runs. Note that  
 182 since the process is stochastic, the variance in the number of particles ejected per inci-  
 183 dent particle will not change much if even more impacts are simulated. The sputtering  
 184 yield predicted by Eq. 1 is in blue for iron and purple for quartz. The sputtering yield  
 185 from Eq. 1 is at most a factor of two off from the average sputtering yield found in the  
 186 simulations. In all cases the model falls within a standard deviation of the average sim-  
 187 ulation result.

191 While Bohdansky, Lindner, Hechtel, Martinelli, and Roth (1986) found sputtering  
 192 yield to be independent of temperature in a lab, Behrisch and Eckstein (1993) found a  
 193 30% increase in yield near sublimation temperatures for silver. Meteoroids heat as they  
 194 descend into the atmosphere, so the sputtering and energy transfer from incident atmo-  
 195 spheric particles with higher temperature targets warrants further investigation. Pre-  
 196 liminary simulations with meteoroid targets at higher temperature, which will be reported  
 197 in future work, suggest that the yield and energy transfer remain approximately the same  
 198 for hotter targets, though this could change if the target has a surface in another phase.

### 199 2.3 Angular Dependence of Sputtering Yield

200 The simulations in Sec. 2.2 study impacts normal incidence, but particles will im-  
 201 pact a meteoroid at a range of angles depending on the shape of the meteoroid. In this  
 202 section, we examine the angular dependence. Sputtering yield models often define the  
 203 yield at normal incidence (e.g. Eq. 1) and describe the angular dependence as a func-



188 **Figure 3.** Sputtering yield at normal incidence for Ar (red), O<sub>2</sub> (orange), and N<sub>2</sub> (green)  
 189 impacts on iron in the first row and quartz in the second, with 2 lines denoting one and two  
 190 standard deviations above the mean. The blue (iron) or purple (quartz) line is the model (Eq. 1).

204 tion of the yield at normal incidence. Draine and Salpeter (1979) argue that  $\langle Y(E_0, \theta) \rangle \approx$   
 205  $2Y(E_0, \theta = 0)$ . Common approximations for the angular dependence are  $Y(E_0, \theta)/Y(E_0, 0) =$   
 206  $\cos^{-1} \theta$  at lower energies (Almén & Bruce, 1961; Molchanov & Telkovski, 1961; Sigmund,  
 207 1969; Draine & Salpeter, 1979; Rogers et al., 2005; Vondrak et al., 2008) and  $Y(E_0, \theta)/Y(E_0, 0) =$   
 208  $\cos^{-1.6} \theta$  at higher energies (Jurac et al., 1998). These forms have a clear problem in that  
 209 they diverge for large angles ( $\theta \rightarrow \pi/2$ ).

Eckstein and Preuss (2003) provide an empirical fit for sputtering yield as a func-  
 tion of angle:

$$\frac{Y(E_0, \theta_0)}{Y(E_0, 0)} = \left\{ \cos \left[ \left( \frac{\pi \theta_0}{2 \theta_0^*} \right)^c \right] \right\}^{-f} \exp \left( b \left\{ 1 - 1 / \cos \left[ \left( \frac{\pi \theta_0}{2 \theta_0^*} \right)^c \right] \right\} \right), \quad (5)$$

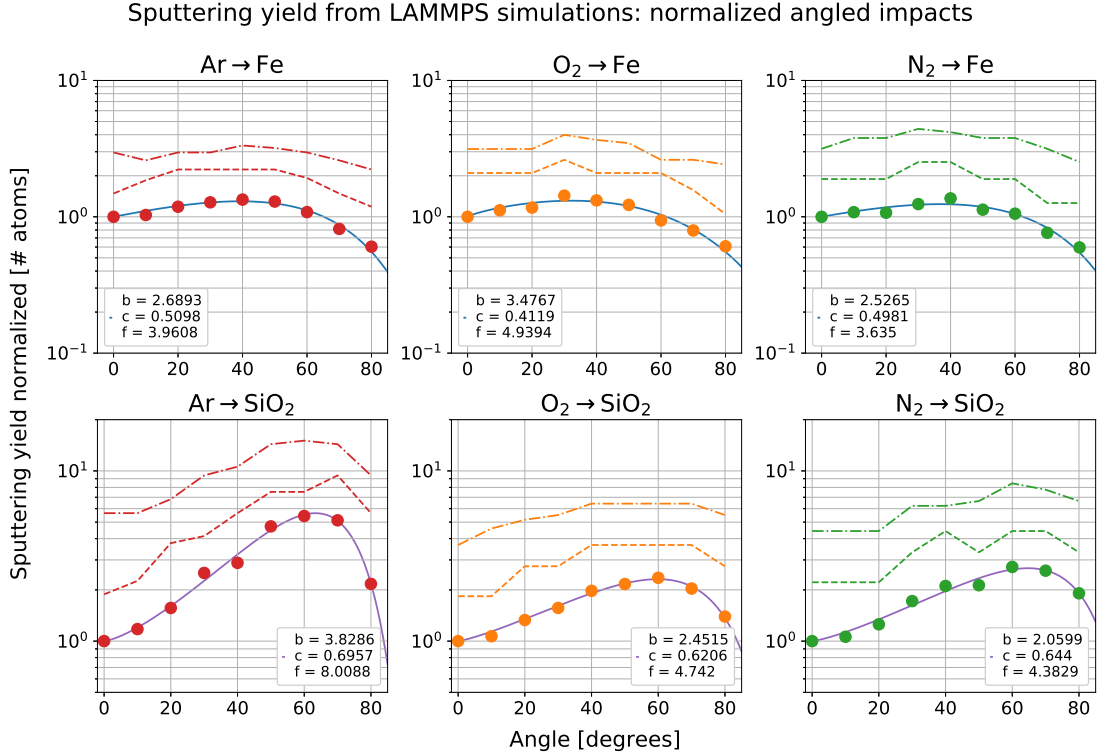
where  $b$ ,  $c$ , and  $f$  are parameters to fit to experimental data. The variable  $\theta_0^*$ , which is  
 given by

$$\theta_0^* = \pi - \arccos \left( \sqrt{\frac{1}{1 + \frac{E_0}{E_{sp}}}} \right) \geq \frac{\pi}{2}, \quad (6)$$

210 is a parameter to negate the fact that a particle experiences a binding energy,  $E_{sp}$ , to  
 211 the target, and cannot impact at an angle of 90° due to that non-zero energy of inter-  
 212 action between the projectile and target. For the cases presented here with argon, ni-  
 213 trogen, and oxygen,  $E_{sp} \approx 0$  and  $\theta_0^* \approx \pi$ .

214 To examine the angular dependence of the sputtering yield, we use all of the same  
 215 impactors (argon, nitrogen, and oxygen) and same meteoroid targets (iron and quartz)

216 as the Section 2.2 at a meteoroid velocity of 59.8 km/s. Impact angles vary from  $0^\circ$  to  
 217  $80^\circ$  in  $10^\circ$  degree increments. For impacts at large angles, the simulations take consid-  
 218 erably longer to resolve (up to 36 ps) compared to impacts at normal incidence (4 ps).  
 219 Fig. 4 shows the angular dependence relative to the sputtering yield at normal incidence.  
 220 We fit the simulation results to Eq. 5 for each case and list the parameters  $b$ ,  $c$ , and  $f$   
 221 in legend of the Figure.



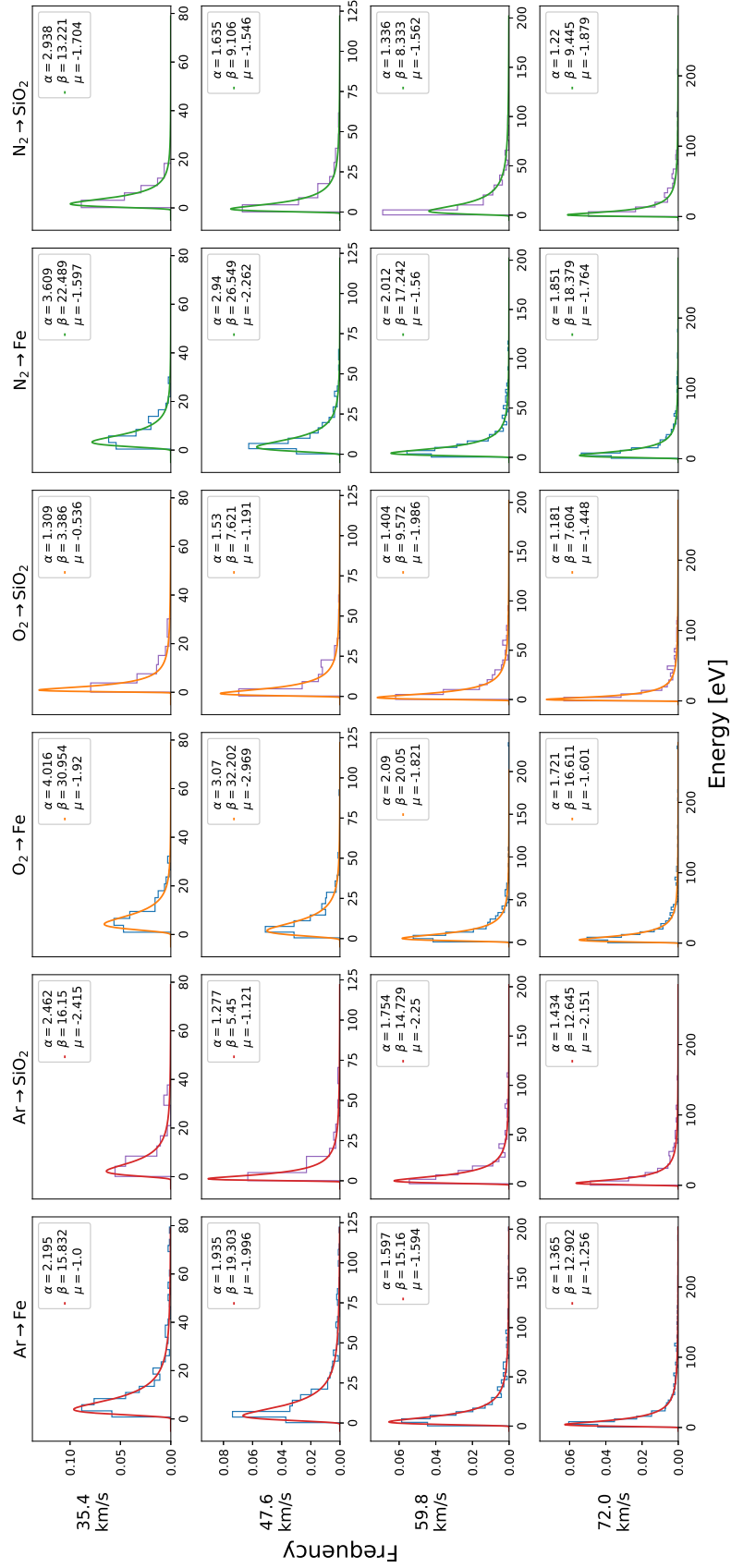
222 **Figure 4.** Sputtering yield versus angle for Ar, O<sub>2</sub>, and N<sub>2</sub> impacts on iron in the top row  
 223 and quartz on the bottom, normalized to  $Y(E_0, 0)$ . The two lines denote one and two standard  
 224 deviations above the mean. The blue (iron) or purple (quartz) line is the Eq. 5, with the param-  
 225 eters in the legend

## 226 2.4 Sputtered Energy

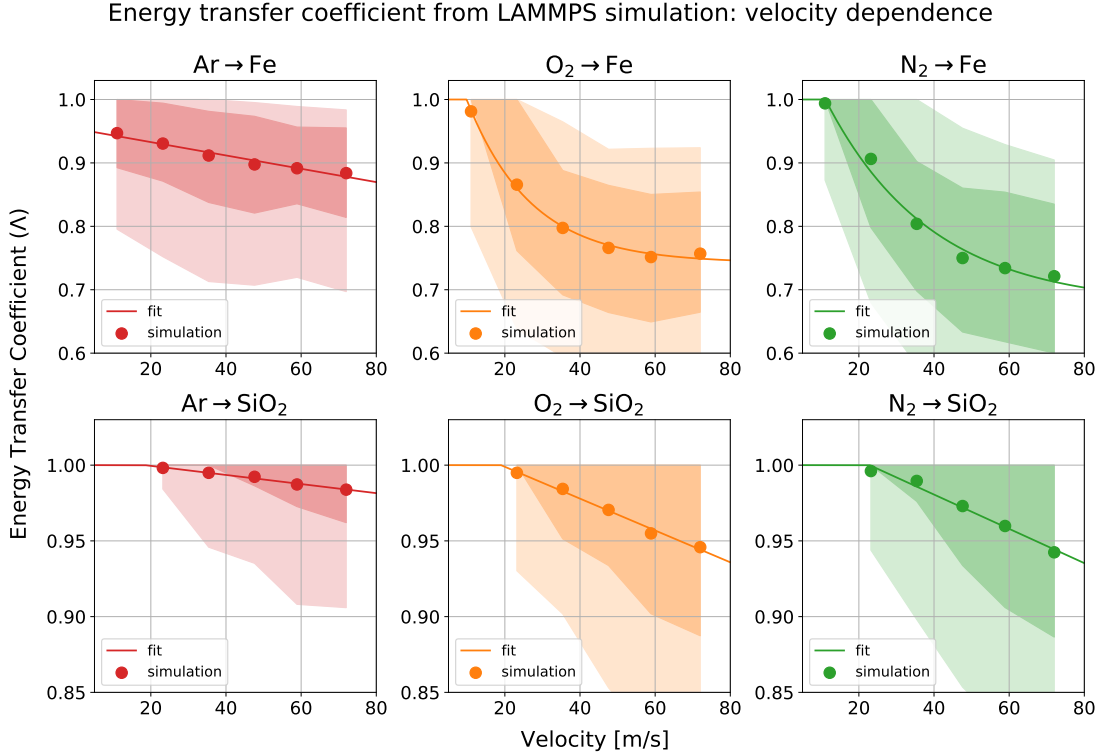
227 MD simulations track the sputtered particle energies. The kinetic energy the par-  
 228 ticle in the last time-step within the bounds of the simulation defines the sputtered par-  
 229 ticle energy. At the point where a sputtered or reflected particle crosses the boundary,  
 230 there is no interaction with the meteoroid atoms and its kinetic energy is constant. Record-  
 231 ing the sputtered particle energies for each impact velocity and composition combina-  
 232 tion provides data for energy distribution histograms.

235 Figure 5 shows the distribution of the sputtered particle energy from Ar, O<sub>2</sub>, and  
 236 N<sub>2</sub> impacts on iron and quartz. More sputtering events occur at higher initial energies,  
 237 given by Eq. 1, and therefore more overall entries in the histogram. The lower energy  
 238 impacts have orders of magnitude smaller sputtering yields resulting in less total data  
 239 from the same number of trials. The inverse gamma distribution is characterized by a  
 240 steep initial rise, skewed shape, and the long tail that closely fit the histograms in Fig. 5.  
 241 The parameters of the distribution (found in the legends in Fig. 5) are the shape param-

Energy distribution of sputtered atoms from LAMMPS simulation



233 **Figure 5.** Histograms of energies of the sputtered particles from Ar, O<sub>2</sub> and N<sub>2</sub> impact. The  
 234 parameters in the legends are the shape, scale, and location fit parameters.



250 **Figure 6.** Energy as a function of angle for Ar, O<sub>2</sub>, and N<sub>2</sub> impacts on iron and quartz, with  
 251 fit for each atmospheric particle. The darker inner section is one standard deviation, and the  
 252 lighter outer region is two standard deviations.

242 eter  $\alpha$ , the scale parameter  $\beta$ , and location parameter  $\mu$ . This probability distribution  
 243 function was chosen over other PDFs like the Maxwell-Boltzmann distribution or the Gamma  
 244 distribution simply due to its smaller residual value when fitting the simulation data.

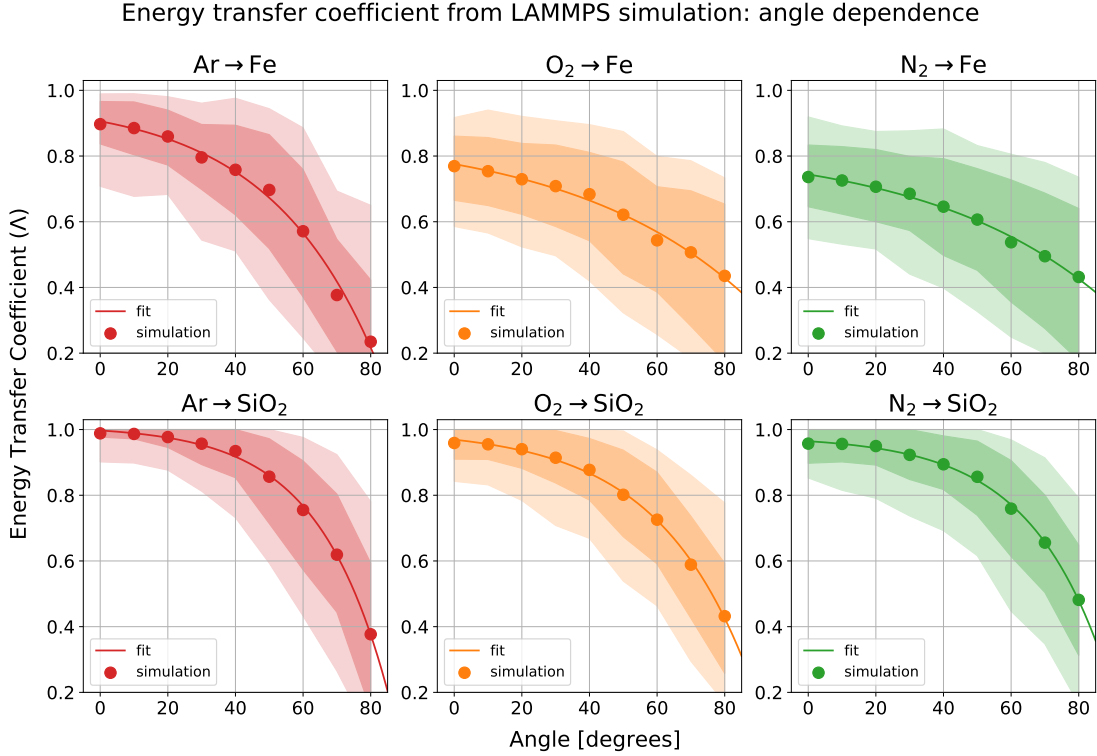
## 245 2.5 Energy Transfer

The energy transfer is the fraction of the initial energy of the atmospheric particle transferred into the meteoroid surface. In this section, this coefficient refers to a single impact. Taking  $E_i$ , the initial energy of the atmospheric particle, and subtracting  $\Sigma E_s$ , the energies of any ricocheted atmospheric and sputtered particles from the LAMMPS simulations, gives the energy transferred to the meteoroid atoms. The increased energy kinetic energy of the meteoroids is equivalent to increased temperature of the meteoroid. The energy transfer coefficient is

$$\Lambda = \frac{E_i - \Sigma E_s}{E_i} \quad (7)$$

246 and characterizes the efficiency of energy transfer (and thus heating) based on a single  
 247 impact. The energy transfer coefficient depends on velocity, angle, and projectile species.  
 248 The simulation provides  $\Sigma E_s$  based on an input  $E_i$ , and the details of the atomic inter-  
 249 actions, including energy lost to breaking bonds, are included in the MD simulation.

253 Fig. 6 shows the energy transfer coefficient for normal impacts of Ar, N<sub>2</sub> and O<sub>2</sub>  
 254 on iron and quartz as a function of velocity. The sputtered atoms tend to play the small-  
 255 est role in energy loss because ricocheting atmospheric atoms carry away most of the lost  
 256 energy. The impacts on iron meteoroids have larger  $\Lambda$  on average because the iron lat-



268 **Figure 7.** Energy transfer coefficient as a function of angle for Ar, O<sub>2</sub>, and N<sub>2</sub> impacts on  
 269 iron and quartz. The darker inner section is one standard deviation, and the lighter outer region  
 270 is two standard deviations.

257 tice is more compact and tends to reflect the incident atmospheric particle more often.  
 258 The energy transfer coefficient is closer to 1 for quartz due to the crystal structure. The  
 259 atmospheric particles embed themselves in the quartz surface more often due to the large  
 260 gaps in the crystalline structure. O<sub>2</sub> and N<sub>2</sub> are similar in weight and chemical compo-  
 261 sition, and the bond dissociation energy is 5.165 eV for O<sub>2</sub> and 9.799 eV for N<sub>2</sub> (Darwent,  
 262 1970) (there is no bond energy for Ar, which is monatomic). The energy of the ricochet-  
 263 ting nitrogen and oxygen atoms increases with initial energy, but at a slower rate than  
 264 the decreasing fraction the bond dissociation energy in the total initial energy. There-  
 265 fore the energy transfer coefficient of O<sub>2</sub> and N<sub>2</sub> decreases sharply at with increasing en-  
 266 ergy at the lowest energies, and (with lessening relevance of the bond energy) levels off  
 267 at higher energies.

271 Fig. 7 shows the energy transfer coefficient as a function of impact angle. The en-  
 272 ergy transfer coefficient decreases with increasing angle. As the impacting particle's trans-  
 273 verse energy increases (i.e. angle increases), it often bounces off the surface, imparting  
 274 little energy as it ricochets. Applying these simulation results to determine  $\Lambda$  requires  
 275 averaging over the angle and assuming a meteoroid shape. This is addressed in Section  
 276 3.2 below.

### 277 3 Ablation Model with a Modified Energy Transfer Coefficient

278 The LAMMPS simulations from the previous section provide the energy transfer  
 279 coefficient as a function of velocity, material and angle. Applying the energy transfer co-  
 280 efficient results, we model the evolution of a meteoroid as it descends into the atmosphere

281 using numerical meteoroid ablation model. Ablation models predict visual magnitude  
 282 and electron line density, corresponding to optical and radar measurements respectively,  
 283 from the ablation model output. Integrating over the surface of the meteoroid results  
 284 in the energy transfer coefficient as a function of velocity and altitude.

### 285 3.1 Ablation Model

286 Sublimation is the final and the largest driver of meteoroid mass loss. Once the me-  
 287 teoroid has reached sublimation (sometimes referred to as thermal ablation) tempera-  
 288 tures, the meteoroid begins to sublimate. Most meteoroids sublimate entirely into the  
 289 atmosphere before striking the ground. The four coupled ordinary differential equations  
 290 described below model this process. These equations follow work from Campbell-Brown  
 291 and Koschny (2004), Rogers et al. (2005), and Vondrak et al. (2008).

292 The mass loss as a function of time resulting from sputtering (the first term) and  
 293 sublimation (the second term),

$$\frac{dm}{dt} = -\left(\frac{3m\pi^{1/2}}{4\rho_m}\right)^{2/3} M_2 v \sum_i n_i Y_i(E_0, \theta)_i - \left(\frac{3m\pi^{1/2}}{4\rho_m}\right)^{2/3} \psi p_s \sqrt{\frac{\mu}{2\pi k_b T}} \quad (8)$$

where,  $m$  is the meteoroid mass,  $\rho_m$  is the meteoroid mass density,  $v$  is the velocity, and  
 $n_i$  and  $Y_i$  are the atmospheric number density and the sputtering yield of the  $i$ -th at-  
 mospheric species respectively.  $M_2$  in the sputtering mass loss term is the meteoroid's  
 average atomic mass, whereas  $\mu$  is the meteoroid's average molecular mass, as sputter-  
 ing dislodges single atoms and sublimation ejects entire molecules. The sublimation term  
 uses the Clausius- Clapeyron equation for saturated vapor pressure,  $p_s$ , defined as

$$p_s = \exp\left(C - \frac{L\mu}{k_b T}\right) \quad (9)$$

294 where  $L$  is the latent heat of evaporation and  $C$  is a material dependent constant.  $\psi$  is  
 295 the condensation probability coefficient,  $k_b$  is the Boltzmann constant, and  $T$  is the me-  
 296 teoroid temperature. The sublimation mass loss term primarily depends on the temper-  
 297 ature of the meteoroid. Once the meteoroid has reached evaporation temperatures,  $p_s$   
 298 mainly governs how much mass is ejected during this stage of ablation.

The change in temperature of the meteoroid comes from conservation of energy,  
 given by

$$\frac{1}{2} \Lambda \rho_{air} v^3 = 4\epsilon\sigma(T^4 - T_{air}^4) + \frac{c(m\rho_m^2)^{1/3}}{A} \frac{dT}{dt} - \frac{L}{A} \left(\frac{m}{\rho_m}\right)^{2/3} \frac{dm}{dt}_{sub} \quad (10)$$

299 The left hand side is the energy from the atmospheric particles. The energy transfer co-  
 300 efficient,  $\Lambda$ , is discussed in Section 2.5. The right hand side represents the energy lost  
 301 to thermal radiation, meteoroid heating, and sublimation, respectively. In the radiation  
 302 term,  $\epsilon$  is the emissivity of the meteoroid,  $\sigma$  is Stefan-Boltzmann's constant, and  $T_{air}$   
 303 is the atmospheric temperature. In the heating term,  $c$  is the specific heat of the mete-  
 304 oroid, and  $dT/dt$  is the meteoroid temperature change as a function of time. In the sub-  
 305 limation term,  $\frac{dm}{dt}_{sub}$  is the mass loss due to sublimation (the second term in Eq. 8).

The deceleration of the meteoroid,

$$\frac{dv}{dt} = -\frac{\Gamma A}{(m\rho_m^2)^{1/3}} \rho_{air} v^2 \quad (11)$$

comes from conservation of linear momentum of an object moving through a fluid.  $\Gamma$  is  
 the drag coefficient, describing the efficiency of momentum transfer from atmospheric

particle impacts. The the change in altitude as a function of time is given by

$$\frac{dh}{dt} = -v \cos(\chi) \quad (12)$$

306 where  $\chi$  is the angle of entry into the atmosphere.

The intensity of the radiation the meteoroid produces as it ablates is given by

$$I = -\frac{1}{2}\tau_1 v^2 \frac{dm}{dt}. \quad (13)$$

The luminous efficiency factor,  $\tau_1$ , is defined as

$$\tau_1 = 2\frac{\epsilon}{\mu} \frac{\zeta}{v^2} \quad (14)$$

where  $\epsilon$  is the mean excitation energy, and  $\mu$  is the molecular mass, and  $\zeta$ , the excitation coefficient, is the sum of the excitation probabilities from atomic collisions (Jones & Halliday, 2001; Hill et al., 2005). The relationship between apparent visual magnitude and intensity is given by (Campbell-Brown & Koschny, 2004)

$$m_v = 6.8 - 1.086 \ln I \quad (15)$$

Meteor radars detect the electron line density along the meteor path. The electron line density is defined in Jones (1997) as

$$q = \frac{\beta}{\mu v} \frac{dm}{dt}. \quad (16)$$

In Eq. 16,  $\mu$  is the average ablated particle mass and  $dm/dt$  is the mass loss from Eq. 8. The  $\beta$  term is the ionization coefficient of an atom or molecule, and is a function of velocity, given by

$$\beta(v) = \beta_0(v) + 2 \int_{v_0}^v \beta_0(v') dv' \quad (17)$$

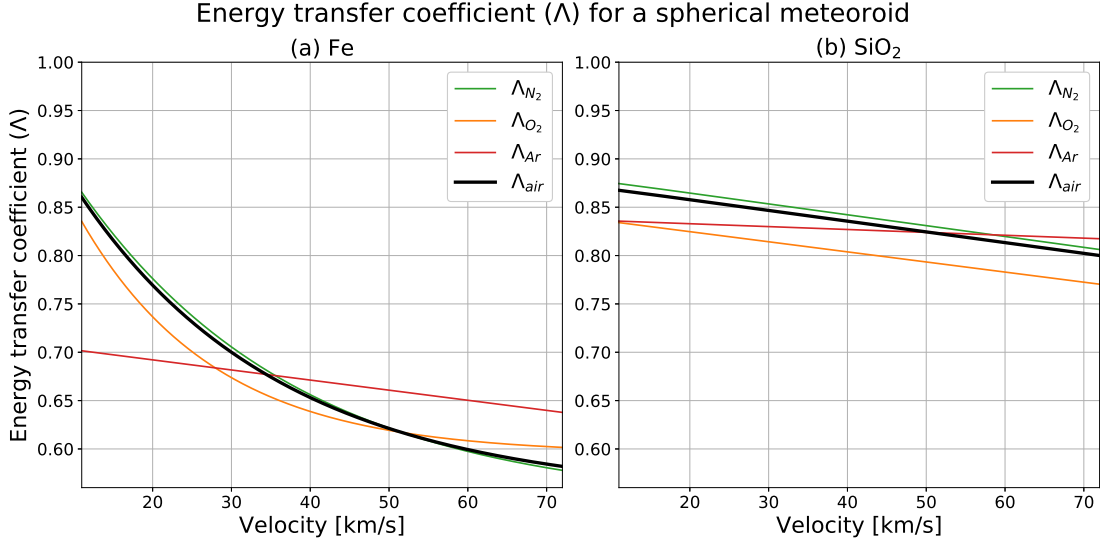
307 where  $\beta_0$  is the ionization probability of a meteoroid particle initial collision with an at-  
308 mospheric particle (Jones, 1997).

309 Electron line density inferred from and visual magnitude are physical observables.  
310 Therefore solving Equations 8, 11, 10, 12, 15 and 16 simultaneously approximately mod-  
311 els the evolution of a meteoroid traveling through an atmosphere. The modeled the vi-  
312 sual magnitude can be compared to light curves of actual meteoroids and electron line  
313 density can be compared to radar measurements.

### 314 **3.2 Microscopic Impacts to Macroscopic Meteoroid interactions**

315 MD simulations in Section 2.5 provided the energy transfer coefficients ( $\Lambda$ ) for sin-  
316 gle impacts at various velocities and angles. Integrating  $\Lambda$  from the simulations across  
317 a spherical meteoroid surface, taking into account impacts from all angles 0-90°, yields  
318 the energy transfer coefficient,  $\langle \Lambda(v) \rangle_\theta$ , in Eq. 10 for each particle species, impacting ei-  
319 ther an iron or quartz meteoroid. Fig. 8 shows  $\Lambda$  values of impacts on a spherical me-  
320 teoroid, for the atmospheric species N<sub>2</sub>, O<sub>2</sub>, and Ar, calculated in this manner. The black  
321 line in Fig. 8 is the energy transfer coefficient as a function of velocity using atmospheric  
322 density ratios at 100km altitude.

327 The assumption that the angle averaged sputtering yield,  $\langle Y(E) \rangle_\theta$ , is twice the nor-  
328 mal yield, is often used while solving for the sputtering portion of the mass loss term in  
329 numerical models (Draine, 1977; Draine & Salpeter, 1979; Rogers et al., 2005; Vondrak  
330 et al., 2008; Briani et al., 2013). The MD simulations suggest this can be inaccurate, es-  
331 pecially for iron. We found that the angle averaged sputtering yield for Argon, O<sub>2</sub>, and



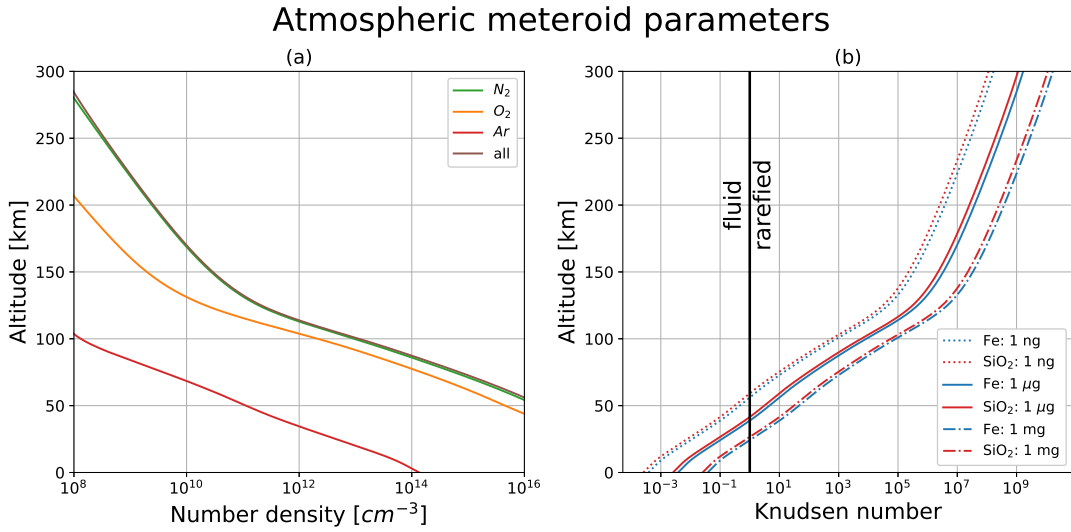
323 **Figure 8.** The energy transfer coefficient,  $\Lambda$ , as a function of velocity for both iron and quartz  
 324 determined from MD simulations in Section . The three atmospheric species are in red, green,  
 325 and orange, with the black line denoting the thermal energy transfer coefficient of air at 100 km  
 326 altitude.

332  $N_2$  impacting iron is 1.137, 1.124 and 1.088 times the sputtering yield of normal impacts  
 333 respectively. For quartz, we found the angle averaged yield for the same particles is 3.466,  
 334 1.840, and 2.018, respectively.

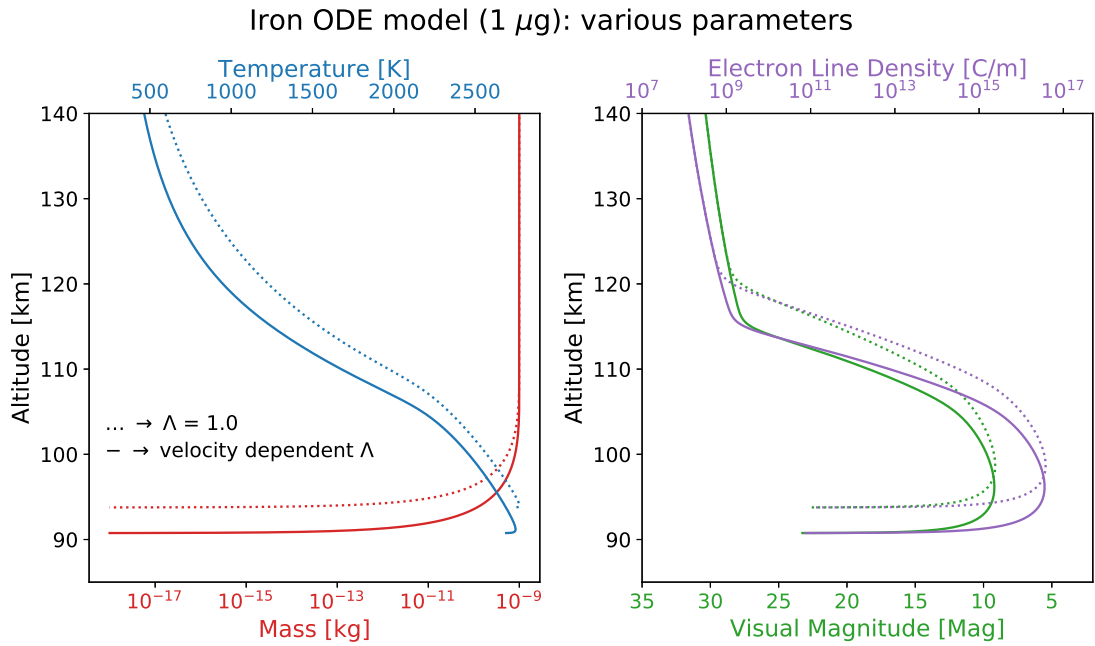
335 Our model uses atmospheric parameters from MSISE20000, (Picone et al., 2002),  
 336 and  $\Lambda$  used in Eq. 10 depends on atmospheric composition. Fig. 9a displays the number  
 337 density from NRLMSISE-00 from 0 to 300 km. Fig. 9b shows the Knudsen number  
 338 as a function of altitude for a range of meteoroids. The Knudsen number is  $Kn = \lambda/L$ ,  
 339 where  $\lambda$  is the mean free path of the atmosphere and  $L$  is the characteristic length of  
 340 the meteoroid. For typical ablation altitudes and small meteoroids  $Kn \gg 1$ , which means  
 341 the meteoroid experiences individual impacts of atmospheric particles instead of fluid  
 342 drag (Sharipov, 2007). This justifies treating the impacts as separate and summing their  
 343 effects.

346 Eqs. 8-12 were solved using a variable-coefficient solver with a fixed-coefficient back-  
 347 ward differentiation formula applicable to stiff problems. We solved the equations twice  
 348 for each initial condition, once with  $\Lambda = 1$ , and once  $\Lambda$  calculated as a function of ve-  
 349 locity and atmospheric composition. Initial masses ranged from  $1 \times 10^{-12}$  kg to  $9 \times 10^{-6}$   
 350 kg and velocities ranged from 11 km/s to 72 km/s. The models used the same veloci-  
 351 ties as in the MD simulations, and 5 different masses per order of magnitude.

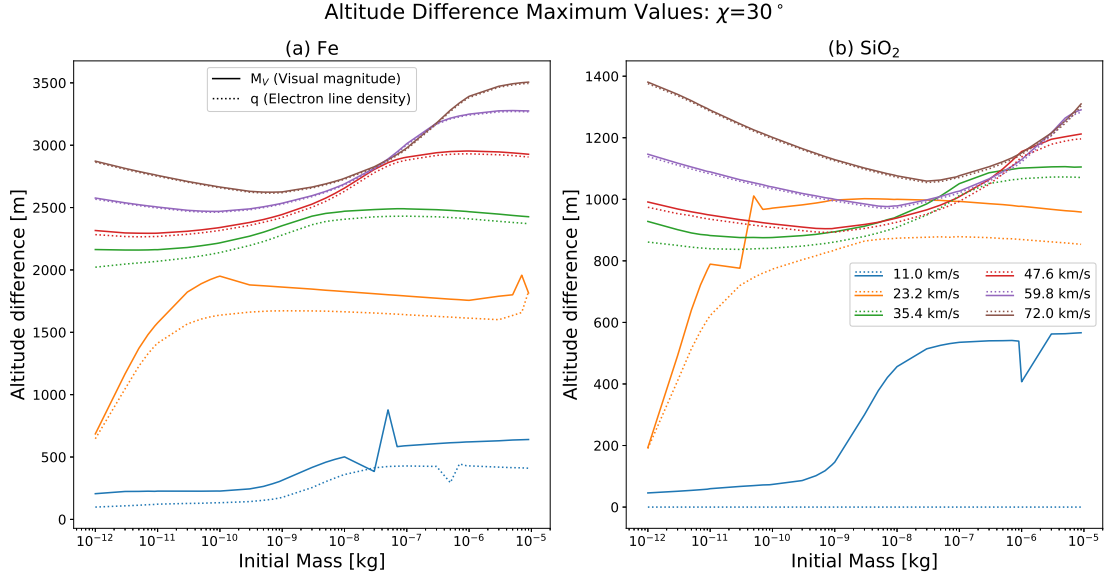
352 Fig. 10 shows the results from the ablation model for an iron meteoroid with and  
 353 initial mass of  $1 \mu\text{g}$  and velocity of 59.8 km/s. The dotted line sets  $\Lambda = 1$  and the solid  
 354 line uses the calculated  $\Lambda < 1$ . The meteoroid heats at a slower rate with  $\Lambda < 1$  as  
 355 expected.  $\Lambda$  is 15-40% lower for iron and 10-25% lower for stony meteoroids. The slower  
 356 heating rate affects the rate of mass loss, the visual intensity (Eq. 15), in purple, and the  
 357 electron line density (Eq. 16), in green. In Fig. 10 the altitude of the maximum visual  
 358 magnitude and electron line density differs by 2.5km with different  $\Lambda$ .



344 **Figure 9.** Atmospheric parameters with species and total number density from 0 to 300 km in  
 345 altitude (a) and Knudsen number for different meteoroids (b).



359 **Figure 10.** Results from the ablation model for an iron meteoroid with an initial mass of 1  
 360  $\mu\text{g}$  and initial velocity of 59.8 km/s. The left plot shows meteoroid temperature and mass, with  
 361 the dotted line indicating the model with  $\Lambda=1.0$  and the solid line indicating the model with  
 362  $\Lambda < 1$ . The right plot shows visual magnitude and electron line density as calculated by Eq. 15  
 363 and Eq. 16 respectively.



372 **Figure 11.** Relationship between altitude difference of the maximum value of visual mag-  
 373 nitude and electron line density, and the initial masses, of the numerical model where  $\Lambda = 1$  and  
 374  $\Lambda < 1$ . The solid line and the dotted line is the altitude difference for visual magnitude ( $M_V$ )  
 375 and the electron line density ( $q$ ) respectively. The figure on the left show the results for an iron  
 376 meteoroid and on the right show the results for a quartz meteoroid.

### 364 3.3 Observable Parameters

365 We compare the effect of the simulation-derived energy transfer coefficient to the  
 366 assumption that  $\Lambda = 1$  by contrasting the altitude of maximum values of the visual mag-  
 367 nitude and electron line density from the ablation model. The meteoroid masses range  
 368 from the largest meteoroid in the valid free-molecular flow regime ( $10^{-6}$  kg) to the small-  
 369 est meteoroids detectable by radar ( $10^{-12}$  kg). Fig. 11 shows the difference in altitude  
 370 of the maximum visual magnitude and electron line density between the  $\Lambda = 1$  and the  
 371  $\Lambda < 1$  solutions.

377 In Fig. 11 show the altitude difference of the electron line density and visual mag-  
 378 nitude respectively for iron quartz meteoroids. The infrequent departures from smooth-  
 379 ness are a result of imperfect interpolation of atmospheric parameters to the meteoroid  
 380 location at any given time. The change in altitude for quartz is less than for iron because  
 381 the energy transfer coefficient for quartz is closer to one, because it loses less energy to  
 382 ricochet and sputtered particles, as shown in Sec. 2.5.

383 Quartz's threshold velocity for ionization is around 12.9 km/s, so the electron line  
 384 density from the 11.0 km/s run is zero across all masses. Otherwise in Fig. 11b the al-  
 385 titude difference is fairly constant across the masses, and tends towards a difference of  
 386 1000-1300 meters. Lower initial velocities (11.0 and 23.2 km/s) have smaller altitude dif-  
 387 ferences due to the meteoroids decelerating to below the threshold velocities for visual  
 388 magnitude, (6.8 km/s, per the relation for  $\eta$  in Eq. 14). The altitude difference in elec-  
 389 tron line density and visual magnitude begins to diminish at the threshold velocity more  
 390 quickly at 23.2 for masses over  $1\mu\text{g}$  due to the  $m^{-1/3}$  factor in Eq. 11.

391 Iron's three fastest velocities' altitude differences group together between 2500 and  
 392 3500 meters. This occurs because of the small range of the energy transfer coefficient at

393 higher velocities for N<sub>2</sub> and O<sub>2</sub> in Fig. 6 results in similar heating rates. The smallest  
 394 initial masses, especially at high velocities, sublimate very quickly. This results in the  
 395 high velocity altitude differences decreasing from 10<sup>-12</sup> kg to 10<sup>-9</sup>kg. The increase in  
 396 the altitude differences for heavier meteoroids comes from the duration sputtering pe-  
 397 riod. The maximum rate of mass loss occurs right at the beginning of sublimation. The  
 398 heating rate (determined by the energy transfer coefficient) determines the duration of  
 399 sputtering period and the altitude where the meteoroid begins sublimation. The sput-  
 400 tering period increases with mass as the heavier meteoroids require more impacts to reach  
 401 sublimation temperatures than smaller meteoroids or their  $\Lambda = 1$  counterparts.

## 402 4 Conclusions

403 Molecular dynamics simulation of atomic scale sputtering on the surface of mete-  
 404 oroids due to atmospheric particle impacts show how energy transfer from the atmosphere  
 405 depends on the species, velocity, angle, and meteoroid material. Single particle impacts  
 406 are important not only for sputtering, but for sublimation as well, since the dynamics  
 407 of the single impacts govern how quickly a meteoroid gains thermal energy. Applying  
 408 a more accurate energy transfer coefficient adds an additional level of accuracy to mod-  
 409 els of meteoroid ablation in the atmosphere. Here we present our main conclusions, both  
 410 from the MD simulations and the numerical ablation models:

- 411 1. Sputtering yield at normal incidence found by the LAMMPS simulations follows  
 412 the incident energy dependent equation put forth by Tielens et al. (1994) within  
 413 a factor of 2 for iron and an order of magnitude for quartz.
- 414 2. Sputtering yield at various angles was found to best fit the empirical normalized  
 415 yield equation from Eckstein and Preuss (2003), which differs greatly from gen-  
 416 erally assumed distributions (e.g. Jurac et al. (1998), Rogers et al. (2005)).
- 417 3. The MD data shows that the impacting energy is not entirely incorporated into  
 418 the meteoroid as assumed in many ablation models. Instead, the energy transfer  
 419 coefficient depends on incident velocity and meteoroid material.
- 420 4. Applying the newly derived energy transfer coefficient to the ablation model pre-  
 421 dict that observable parameters reach their peak at lower altitudes (3.5 km dif-  
 422 ference for iron and 1.3 km difference for quartz).

423 Currently, we lack a complete profile of meteoroid energy transfer coefficients, as  
 424 we did not examine the temperature dependence. Future work will involve using MD sim-  
 425 ulations to model meteoroids with elevated temperatures and the sublimation process.  
 426 This will allow us to determine temperature dependent sputtering rates and energy trans-  
 427 fer coefficient.

## 428 Acknowledgments

429 This work is supported by NSF Grant AGS-1755020, NSF Grant AGS-1755350, NSF-  
 430 AGS Postdoctoral Research Fellowship Award No. 143353, Naval Research Laboratory  
 431 Base Program, and the Boston University Undergraduate Research Opportunities Pro-  
 432 gram. This work used the Extreme Science and Engineering Discovery Environment (XSEDE),  
 433 which is supported by National Science Foundation grant ACI-1548562. The authors ac-  
 434 knowledge the Texas Advanced Computing Center (TACC) at The University of Texas  
 435 at Austin for providing HPC resources that have contributed to the research results re-  
 436 ported within this paper; URL: <http://www.tacc.utexas.edu>. Data is available online (<https://doi.org/10.7910/DV>)

## 437 References

- 438 Almén, O., & Bruce, G. (1961). Collection and sputtering experiments with  
 439 noble gas ions. *Nucl. Instrum. Methods*, 11, 257–278. Retrieved from

- 440 <http://www.sciencedirect.com/science/article/pii/0029554X6190026X>  
 441 doi: [https://doi.org/10.1016/0029-554X\(61\)90026-X](https://doi.org/10.1016/0029-554X(61)90026-X)
- 442 Behrisch, R., & Eckstein, W. (1993). Sputtering yield increase with target tem-  
 443 perature for ag. *Nucl. Instrum. Methods Phys. Res. B*, 82(2), 255–258. doi:  
 444 [https://doi.org/10.1016/0168-583X\(93\)96027-A](https://doi.org/10.1016/0168-583X(93)96027-A)
- 445 Behrisch, R., & Eckstein, W. (2007). *Sputtering by particle bombardment: Experi-*  
 446 *ments and computer calculations from threshold to mev energies* (Vol. 110).  
 447 Berlin: Springer.
- 448 Berthelot, D. (1898). Sur le mélange des gaz. *C. R. Hebd. Seances Acad.*  
 449 *Sci*, 126(1), 1703–1855. Retrieved from [http://visualiseur.bnf.fr/](http://visualiseur.bnf.fr/CadresFenetre?O=NUMM-3082&I=1703&M=notice)  
 450 [CadresFenetre?O=NUMM-3082&I=1703&M=notice](http://visualiseur.bnf.fr/CadresFenetre?O=NUMM-3082&I=1703&M=notice) doi: 10.1002/andp  
 451 .18812480110
- 452 Bohdanský, J. (1984). A universal relation for the sputtering yield of monatomic  
 453 solids at normal ion incidence. *Nucl. Instrum. Methods Phys. Res. B*, 2(1),  
 454 587–591.
- 455 Bohdanský, J., Lindner, H., Hechtel, E., Martinelli, A., & Roth, J. (1986). Sputter-  
 456 ing yield of cu and ag at target temperatures close to the melting point. *Nucl.*  
 457 *Instrum. Methods Phys. Res. B*, 18(1), 509–514. doi: [https://doi.org/10.1016/](https://doi.org/10.1016/S0168-583X(86)80078-7)  
 458 [S0168-583X\(86\)80078-7](https://doi.org/10.1016/S0168-583X(86)80078-7)
- 459 Bouneau, S., Brunelle, A., Della-Negra, S., Depauw, J., Jacquet, D., Le Beyec, Y.,  
 460 ... Andersen, H. (2002, 03). Very large gold and silver sputtering yields in-  
 461 duced by kev to mev energy au<sub>n</sub> clusters (n = 1-13). *Phys. Rev. B*, 65(14),  
 462 144106-1–144106-8. doi: 10.1103/PhysRevB.65.144106
- 463 Briani, G., Pace, E., N. Shore, S., Pupillo, G., Passaro, A., & Aiello, S. (2013, 02).  
 464 Simulations of micrometeoroid interactions with the earth atmosphere. *Astron.*  
 465 *Astrophys.*, 552, A53. doi: 10.1051/0004-6361/201219658
- 466 Campbell-Brown, M., & Koschny, D. (2004, 05). Model of the ablation of faint mete-  
 467 ors. *Astron. Astrophys.*, 418, 751-758. doi: 10.1051/0004-6361:20041001-1
- 468 Cepelcha, Z., Borovička, J., Elford, W. G., ReVelle, D. O., Hawkes, R. L., Porubčan,  
 469 V., & Šimek, M. (1998). Meteor phenomena and bodies. *Space Sci. Rev.*,  
 470 84(3), 327–471. Retrieved from <https://doi.org/10.1023/A:1005069928850>  
 471 doi: 10.1023/A:1005069928850
- 472 Cheney, K. B., Rogers, E. E., & Pitkin, E. T. (1963, 07). *Research on experimen-*  
 473 *tal evaluation of sputtering yield rates* (Tech. Rep.). MARQUARDT CO VAN  
 474 NUYS CA.
- 475 Darwent, B. (1970). *Bond dissociation energies in simple molecules* (No. 31). U.S.  
 476 National Bureau of Standards. Retrieved from [https://books.google.com/](https://books.google.com/books?id=QoXMY0gi8CkC)  
 477 [books?id=QoXMY0gi8CkC](https://books.google.com/books?id=QoXMY0gi8CkC)
- 478 DeLuca, M., & Sternovsky, Z. (2019). High-speed drag measurements of alu-  
 479 minium particles in free molecular flow. *Journal of Geophysical Research: Space*  
 480 *Physics*, 124(5), 3743–3751. Retrieved from [https://agupubs.onlinelibrary](https://agupubs.onlinelibrary.wiley.com/doi/abs/10.1029/2019JA026583)  
 481 [.wiley.com/doi/abs/10.1029/2019JA026583](https://agupubs.onlinelibrary.wiley.com/doi/abs/10.1029/2019JA026583) doi: 10.1029/2019JA026583
- 482 Dimant, Y. S., & Oppenheim, M. M. (2017a). Formation of plasma around a small  
 483 meteoroid: 1. kinetic theory. *J. Geophys. Res. Space Physics*, 122(4), 4669–  
 484 4696. Retrieved from [https://agupubs.onlinelibrary.wiley.com/doi/abs/](https://agupubs.onlinelibrary.wiley.com/doi/abs/10.1002/2017JA023960)  
 485 [10.1002/2017JA023960](https://agupubs.onlinelibrary.wiley.com/doi/abs/10.1002/2017JA023960) doi: 10.1002/2017JA023960
- 486 Dimant, Y. S., & Oppenheim, M. M. (2017b). Formation of plasma around a small  
 487 meteoroid: 2. implications for radar head echo. *J. Geophys. Res. Space Phys.*,  
 488 122(4), 4697-4711. Retrieved from [https://agupubs.onlinelibrary.wiley](https://agupubs.onlinelibrary.wiley.com/doi/abs/10.1002/2017JA023963)  
 489 [.com/doi/abs/10.1002/2017JA023963](https://agupubs.onlinelibrary.wiley.com/doi/abs/10.1002/2017JA023963) doi: 10.1002/2017JA023963
- 490 Draine, B. T. (1977). Center for radiophysics and space research report no. 669.  
 491 Cornell University.
- 492 Draine, B. T., & Salpeter, E. E. (1979, 8). On the physics of dust grains in hot gas.  
 493 *Astrophys. J.*, 231, 77–94. doi: 10.1086/157165
- 494 Eckstein, W., & Preuss, R. (2003). New fit formulae for the sputtering yield. *J.*

- 495 *Nucl. Mater.*, 320(3), 209–213. Retrieved from [http://www.sciencedirect](http://www.sciencedirect.com/science/article/pii/S0022311503001922)  
 496 [.com/science/article/pii/S0022311503001922](http://www.sciencedirect.com/science/article/pii/S0022311503001922) doi: [https://doi.org/](https://doi.org/10.1016/S0022-3115(03)00192-2)  
 497 [10.1016/S0022-3115\(03\)00192-2](https://doi.org/10.1016/S0022-3115(03)00192-2)
- 498 Elliott, R. S. (2018). *Efficient 'universal' shifted lennard-jones model for all kim*  
 499 *api supported species developed by elliot and akerson (2015) v003*. OpenKIM.  
 500 (Online; accessed: 2019-03-24) doi: 10.25950/962b4967
- 501 Hill, K. A., Rogers, L. A., & Hawkes, R. L. (2005, 12). High geocentric velocity  
 502 meteor ablation. *Astron. Astrophys.*, 444, 615–624. doi: 10.1051/0004-6361:  
 503 20053053
- 504 Jones, W. (1997, 06). Theoretical and observational determinations of the ionization  
 505 coefficient of meteors. *Mon. Notices Royal Astron. Soc.*, 288(4), 995–1003. doi:  
 506 10.1093/mnras/288.4.995
- 507 Jones, W., & Halliday, I. (2001, 02). Effects of excitation and ionization in meteor  
 508 trains. *Mon. Not. R. Astron. Soc.*, 320(4), 417–423. Retrieved from [https://](https://doi.org/10.1046/j.1365-8711.2001.03833.x)  
 509 [doi.org/10.1046/j.1365-8711.2001](https://doi.org/10.1046/j.1365-8711.2001.03833.x) doi: 10.1046/j.1365-8711.2001  
 510 .03833.x
- 511 Jurac, S., Johnson, R. E., & Donn, B. (1998, aug). Monte carlo calculations of  
 512 the sputtering of grains: Enhanced sputtering of small grains. *Astrophys. J.*,  
 513 503(1), 247–252. Retrieved from <https://doi.org/10.10862F305994> doi: 10  
 514 .1086/305994
- 515 Krebs, K. H. (1977). *Investigations on sputtering and secondary ion yield from met-*  
 516 *als under bombardment of noble gases in the energy range 5 - 25kev*. IAEA, Vi-  
 517 enna.
- 518 Laegreid, N., & Wehner, G. K. (1961). Sputtering yields of metals for ar<sup>+</sup> and ne<sup>+</sup>  
 519 ions with energies from 50 to 600 ev. *J. Appl. Phys.*, 32(3), 365–369. Retrieved  
 520 from <https://doi.org/10.1063/1.1736012> doi: 10.1063/1.1736012
- 521 Lebedinets, V. N., & Shushkova, V. B. (1970, 11). Micrometeorite sputtering in the  
 522 ionosphere. *Planet. Space Sci.*, 18, 1653–1659. doi: 10.1016/0032-0633(70)  
 523 90039-5
- 524 Lorentz, H. A. (1881). Ueber die anwendung des satzes vom virial in der kinetis-  
 525 chen theorie der gase. *Ann. Phys. (Berl.)*, 248(1), 127–136. Retrieved from  
 526 <https://onlinelibrary.wiley.com/doi/abs/10.1002/andp.18812480110>  
 527 doi: 10.1002/andp.18812480110
- 528 Love, S. G., & Brownlee, D. E. (1991). Heating and thermal transformation of  
 529 micrometeoroids entering the earth's atmosphere. *Icarus*, 89(1), 26–43.  
 530 Retrieved from [http://www.sciencedirect.com/science/article/pii/](http://www.sciencedirect.com/science/article/pii/0019103591900858)  
 531 [0019103591900858](http://www.sciencedirect.com/science/article/pii/0019103591900858) doi: [https://doi.org/10.1016/0019-1035\(91\)90085-8](https://doi.org/10.1016/0019-1035(91)90085-8)
- 532 Matsunami, N., Yamamura, Y., Itikawa, Y., Itoh, N., Kazumata, Y., Miyagawa,  
 533 S., ... Shimizu, R. (1981). A semiempirical formula for the energy de-  
 534 pendence of the sputtering yield. *Radiat. Eff.*, 57(1–2), 15–21. doi:  
 535 10.1080/01422448008218676
- 536 Molchanov, V. A., & Telkovski, V. G. (1961). The variation of the cathode dis-  
 537 sipation coefficient, as dependent on the angle at which the ions are strik-  
 538 ing the target. *Proc. USSR Acad. Sci.*, 136, 801–802. Retrieved from  
 539 <http://mi.mathnet.ru/dan24584>
- 540 Müller, M., Erhart, P., & Albe, K. (2007, jul). Analytic bond-order potential  
 541 for bcc and fcc iron—comparison with established embedded-atom method  
 542 potentials. *J. Phys. Condens. Matter*, 19(32), 326220. Retrieved from  
 543 <https://doi.org/10.1088/0953-8984/19/32/326220> doi:  
 544 10.1088/0953-8984/19/32/326220
- 545 Munetoh, S., Motooka, T., Moriguchi, K., & Shintani, A. (2007, 4 1). Interatomic  
 546 potential for si-o systems using tersoff parameterization. *Comput. Mater. Sci.*,  
 547 39(2), 334–339. doi: 10.1016/j.commatsci.2006.06.010
- 548 Picone, J. M., Hedin, A. E., Drob, D. P., & Aikin, A. C. (2002). Nrlmsise-00 em-  
 549 pirical model of the atmosphere: Statistical comparisons and scientific issues.

- 550 *J. Geophys. Res. Space Phys.*, 107(A12), SIA 15-1-SIA 15-16. Retrieved  
 551 from [https://agupubs.onlinelibrary.wiley.com/doi/abs/10.1029/](https://agupubs.onlinelibrary.wiley.com/doi/abs/10.1029/2002JA009430)  
 552 2002JA009430 doi: 10.1029/2002JA009430
- 553 Plimpton, S. (1995). Fast parallel algorithms for short-range molecular dy-  
 554 namics. *J. Comput. Phys.*, 117(1), 1–19. Retrieved from [http://](http://www.sciencedirect.com/science/article/pii/S002199918571039X)  
 555 [www.sciencedirect.com/science/article/pii/S002199918571039X](http://www.sciencedirect.com/science/article/pii/S002199918571039X) doi:  
 556 <https://doi.org/10.1006/jcph.1995.1039>
- 557 Plimpton, S. J., & Thompson, A. P. (2012). Computational aspects of many-body  
 558 potentials. *MRS Bulletin*, 37(5), 513–521. doi: 10.1557/mrs.2012.96
- 559 Popova, O. P., Strelkov, A. S., & Sidneva, S. N. (2007). Sputtering of fast mete-  
 560 roids' surface. *Advances in Space Research*, 39(4), 567–573. doi: 10.1016/j.asr  
 561 .2006.05.008
- 562 Rogers, L. A., Hill, K. A., & Hawkes, R. L. (2005). Mass loss due to sputtering  
 563 and thermal processes in meteoroid ablation. *Planet. Space Sci.*, 53(13), 1341  
 564 - 1354. Retrieved from [http://www.sciencedirect.com/science/article/](http://www.sciencedirect.com/science/article/pii/S0032063305001479)  
 565 [pii/S0032063305001479](http://www.sciencedirect.com/science/article/pii/S0032063305001479) doi: <https://doi.org/10.1016/j.pss.2005.07.002>
- 566 Sandia National Labs, & Temple University. (2013). *Overview of lammmps*. Retrieved  
 567 from [https://lammmps.sandia.gov/doc/Intro\\_overview.html](https://lammmps.sandia.gov/doc/Intro_overview.html)
- 568 Sharipov, F. (2007, 01). Rarefied gas dynamics and its applications to vacuum tech-  
 569 nology. *CAS 2006 - CERN Accelerator School: Vacuum in Accelerators, Pro-*  
 570 *ceedings*, 1-13.
- 571 Sigmund, P. (1969, Aug). Theory of sputtering. i. sputtering yield of amor-  
 572 phous and polycrystalline targets. *Phys. Rev.*, 184, 383–416. Retrieved  
 573 from <https://link.aps.org/doi/10.1103/PhysRev.184.383> doi:  
 574 10.1103/PhysRev.184.383
- 575 Szasz, C., Kero, J., Pellinen-Wannberg, A., Meisel, D. D., Wannberg, G., & West-  
 576 man, A. (2008, 6 01). Estimated visual magnitudes of the eiscat uhf meteors.  
 577 *Earth, Moon, and Planets*, 102(1), 373–378.
- 578 Tersoff, J. (1988, 4). New empirical approach for the structure and energy of cova-  
 579 lent systems. *Phys. Rev. B*, 37, 6991–7000. Retrieved from [https://link.aps](https://link.aps.org/doi/10.1103/PhysRevB.37.6991)  
 580 [.org/doi/10.1103/PhysRevB.37.6991](https://link.aps.org/doi/10.1103/PhysRevB.37.6991) doi: 10.1103/PhysRevB.37.6991
- 581 Thomas, E. W. (2017). *Laboratory simulations of micrometeoroid ablation* (PhD  
 582 Dissertation). University of Colorado at Boulder.
- 583 Tielens, A. G. G. M., McKee, C. F., & Seab, H. D. J., C. G. (1994). The physics of  
 584 grain-grain collisions and gas-grain sputtering in interstellar shocks. *Astrophys.*  
 585 *J.*, 431(1), 321–340. doi: 10.1086/174488
- 586 Tsunoyama, K., Suzuki, T., & Ohashi, Y. (1976, 02). Sputtering of iron with ion  
 587 beams of o2+, n2+ and ar+. *Japanese Journal of Applied Physics*, 15(2), 349–  
 588 355. doi: 10.1143/jjap.15.349
- 589 Urbassek, H. M. (1997). Molecular-dynamics simulation of sputtering. *Nu-*  
 590 *clear Instruments and Methods in Physics Research Section B: Beam In-*  
 591 *teractions with Materials and Atoms*, 122(3), 427–441. Retrieved from  
 592 <http://www.sciencedirect.com/science/article/pii/S0168583X96006817>  
 593 (Nanometric Phenomena Induced by Laser, Ion and Cluster Beams) doi:  
 594 [https://doi.org/10.1016/S0168-583X\(96\)00681-7](https://doi.org/10.1016/S0168-583X(96)00681-7)
- 595 Varga, P., Neidhart, T., Sporn, M., Libiseller, G., Schmid, M., Aumayr, F., &  
 596 Winter, H. P. (1997, 01). Sputter yields of insulators bombarded with  
 597 hyperthermal multiply charged ions. *Physica Scripta*, T73, 307–310. doi:  
 598 10.1088/0031-8949/1997/t73/100
- 599 Vida, D., Brown, P. G., & Campbell-Brown, M. (2018, 07). Modelling the measure-  
 600 ment accuracy of pre-atmosphere velocities of meteoroids. *Monthly Notices of*  
 601 *the Royal Astronomical Society*, 479(4), 4307–4319. Retrieved from [https://](https://doi.org/10.1093/mnras/sty1841)  
 602 [doi.org/10.1093/mnras/sty1841](https://doi.org/10.1093/mnras/sty1841) doi: 10.1093/mnras/sty1841
- 603 Vondrak, T., Plane, J. M. C., & Broadley, D., S.; Janches. (2008). A chemical model  
 604 of meteoric ablation. *Atmospheric Chem. Phys.*, 8(23), 7015–7031. doi: 10

605 .5194/acp-8-7015-2008

606 Zhou, L. G., & Huang, H. (2013). Response embedded atom method of interatomic  
607 potentials. *Phys. Rev. B*, *87*(4), 045431. doi: 10.1103/PhysRevB.87.045431

608 Zoerb, K., Williams, J., Williams, D., & Yalin, A. (2005). *Differential sputtering*  
609 *yields of refractory metals by xenon, krypton, and argon ion bombardment at*  
610 *normal and oblique incidences*. The 29th International Electric Propulsion  
611 Conference, Princeton University, New Jersey.